

UC Santa Barbara

UC Santa Barbara Previously Published Works

Title

High-coherence parallelization in integrated photonics.

Permalink

<https://escholarship.org/uc/item/9p5182kp>

Journal

Nature Communications, 15(1)

Authors

Zhang, Xuguang

Zhou, Zixuan

Guo, Yijun

[et al.](#)

Publication Date

2024-09-10

DOI

10.1038/s41467-024-52269-7

Peer reviewed

High-coherence parallelization in integrated photonics

Received: 19 June 2024

Accepted: 28 August 2024

Published online: 10 September 2024

 Check for updates

Xuguang Zhang ^{1,6}, Zixuan Zhou^{1,6}, Yijun Guo^{1,6}, Minxue Zhuang¹, Warren Jin ², Bitao Shen¹, Yujun Chen¹, Jiahui Huang ¹, Zihan Tao¹, Ming Jin ¹, Ruixuan Chen¹, Zhangfeng Ge³, Zhou Fang⁴, Ning Zhang⁴, Yadong Liu⁴, Pengfei Cai⁴, Weiwei Hu¹, Haowen Shu ¹, Dong Pan ⁴, John E. Bowers ² , Xingjun Wang ^{1,3,5}  & Lin Chang ^{1,5} 

Coherent optics has profoundly impacted diverse applications ranging from communications, LiDAR to quantum computations. However, developing coherent systems in integrated photonics comes at great expense in hardware integration and energy efficiency. Here we demonstrate a high-coherence parallelization strategy for advanced integrated coherent systems at minimal cost. By using a self-injection locked microcomb to injection lock distributed feedback lasers, we achieve a record high on-chip gain of 60 dB with no degradation in coherence. This strategy enables highly coherent channels with linewidths down to 10 Hz and power over 20 dBm. The overall electrical-to-optical efficiency reaches 19%, comparable to that of advanced semiconductor lasers. This method supports a silicon photonic communication link with an unprecedented data rate beyond 60 Tbit/s and reduces phase-related DSP consumption by 99.99999% compared to traditional III-V laser pump schemes. This work paves the way for realizing scalable, high-performance coherent integrated photonic systems, potentially benefiting numerous applications.

Integrated photonics has made remarkable progress in providing scalable solutions for communications^{1–5}, computations^{6–9}, quantum information^{10,11} and sensing^{12–14}. To meet the ever-growing capacity and precision requirements posed by these applications, one major evolution trend over the last few years is the adoption of coherent technology in photonic integrated circuits (PICs)^{15,16}. This technology allows for the manipulation of frequency and phase, offering enormous potential for various applications: in communications, the data rate of a transceiver can be lifted by orders of magnitude when replacing the intensity modulation with a coherent scheme^{17–21}; in metrology, high optical coherence enables frequency synthesizing and time keeping with precision beyond 10^{–15}, introducing atomic-level accuracy into PICs²²; in ranging, coherence detection supports FMCW

LiDAR that can simultaneously capture the distance and speed information¹².

However, despite great potential, building a coherent system in integrated photonics has come at a great price in hardware and power consumption. One major difficulty lies in the sources: so far, there is no approach that can generate light with high parallelism, high coherence, and high power simultaneously. The most commonly used source on chip, the III-V distributed feedback (DFB) laser, has excellent power²³ and electrical to optical wall-plug efficiency (WPE)²⁴, but its intrinsic linewidth typically resides at the 100 kHz level, falling short of the coherence requirements in many applications. To achieve better coherence, a commonly adopted method is coupling III-V lasers to high-quality (Q) cavities, which can effectively reduce the linewidth to

¹State Key Laboratory of Advanced Optical Communications System and Networks, School of Electronics, Peking University, Beijing, China. ²Department of Electrical and Computer Engineering, University of California Santa Barbara, Santa Barbara, CA, USA. ³Peking University Yangtze Delta Institute of Optoelectronics, Nantong, China. ⁴SiFotonics Technologies Co., Ltd., Beijing, China. ⁵Frontiers Science Center for Nano-optoelectronics, Peking University, Beijing, China. ⁶These authors contributed equally: Xuguang Zhang, Zixuan Zhou, Yijun Guo. ✉ e-mail: bowers@ece.ucsb.edu; xjwang@pku.edu.cn; linchang@pku.edu.cn

the sub-kHz level. Nevertheless, this sacrifices power and WPE^{25,26}. The high-Q resonator is also used to generate optical frequency combs in parallel coherent systems, but it further worsens both the power and WPE significantly: the nonlinear frequency conversion process usually has an optical-to-optical conversion efficiency at the order of only a few percent^{2,27}. Various methods have recently been developed to improve the conversion efficiency^{28–30}, but the fact that all the comb lines split energies from the pump ultimately limits the channel power, usually below -10 dBm. To leverage such low power in systems, strong amplification with a gain of more than 30 dB is often necessary, posing a challenge for both the integrated erbium-doped fiber amplifier (EDFA)^{4,12} and the semiconductor optical amplifier (SOA)³¹. Meanwhile, both methods inevitably introduce noise into the amplification process. Another way to achieve higher gains is optical injection locking^{32–34}. However, previous works rely on bulky lasers for pumping, which are not compatible with integrated photonic systems. As a result, at the system level, the coherent source still has to rely on expensive benchtop equipment, which is not suitable for scalable applications.

Another challenge for integrated coherent systems is the huge digital signal processing (DSP) consumption^{35,36}. Since the frequency and phase information need to be precisely recovered from the coherent detection, much more DSP is thus required over the intensity-based system. This requirement dramatically increases the power budget and often necessitates dedicated electronics such as DSP chips³⁷. To deploy advanced coherent communication in the next generation data center, DSP chips need to be manufactured with a 3-nm complementary metal-oxide-semiconductor (CMOS) process to

alleviate high power consumption³⁸. Furthermore, the complexity of the DSP makes real-time data processing difficult, as in the LiDAR application. Several attempts have been made to reduce DSP, including laser synchronization³⁹ and cloned combs^{40–42}, but these approaches involve bulky narrow-linewidth sources and desktop phase-locked loops, dramatically adding the hardware burdens at the system level.

In this work, we overcome previous challenges by demonstrating a high-coherence parallelization strategy in integrated photonics. Instead of pushing the efficiency of the coherent light source itself, here we use a high-coherence microcomb as a seed to injection lock (IL) DFB lasers (Fig. 1). We theoretically prove and experimentally demonstrate that this approach can combine the advantages of both the microcomb and the DFB laser, achieving high coherence, high power, and high WPE simultaneously. We show that this strategy can significantly boost the performance of integrated coherent systems by demonstrating a parallel coherent communication experiment using silicon photonic (SiPh) transceivers. We achieve an unprecedented data rate in silicon photonics of over 60 Tbit/s and ease the coherent DSP overhead.

Results

Power-efficient, high-coherence parallel light source on chip

Generating the parallel light source consists of two steps. Firstly, we self-injection lock an indium phosphide DFB laser to a 35 GHz free spectral range Si_3N_4 microresonator with a thickness of 100 nm (Fig. 2a). The Rayleigh backscattering from the microresonator imparts a narrow spectral feedback to the DFB laser and compels the laser to oscillate at the resonance of the microresonator, leading to a

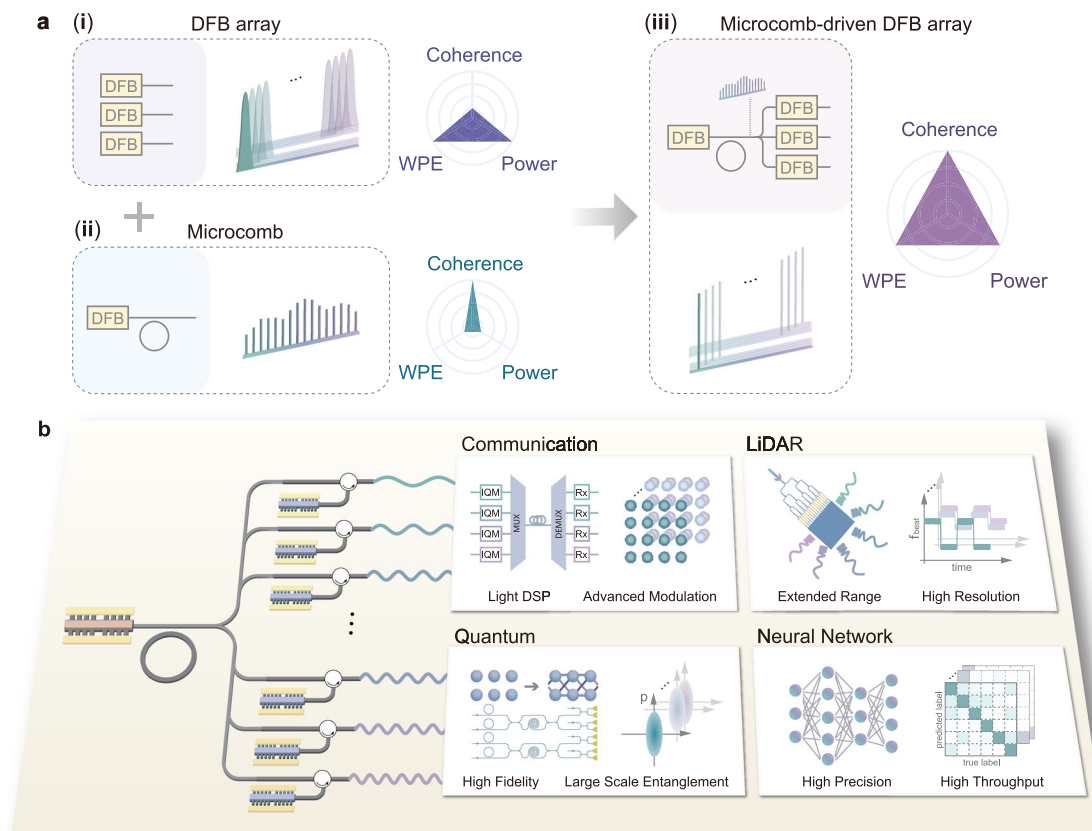


Fig. 1 | High-coherence parallelization based systems. **a** Using a self-injection locked DFB laser, we pump a Si_3N_4 microresonator to generate the microcomb, which is then employed to drive the DFB laser array (**iii**). We can obtain a highly coherent parallel light source that combines the advantages of high power and high WPE of the DFB laser array (**i**) and narrow the linewidth of the microcomb (**ii**).

b Conceptual illustration of the high-coherence parallelization system. This light source can find wide applications in integrated photonic scenarios and exhibits significant potential across various fields, such as communications, LiDAR, quantum information and neural networks.

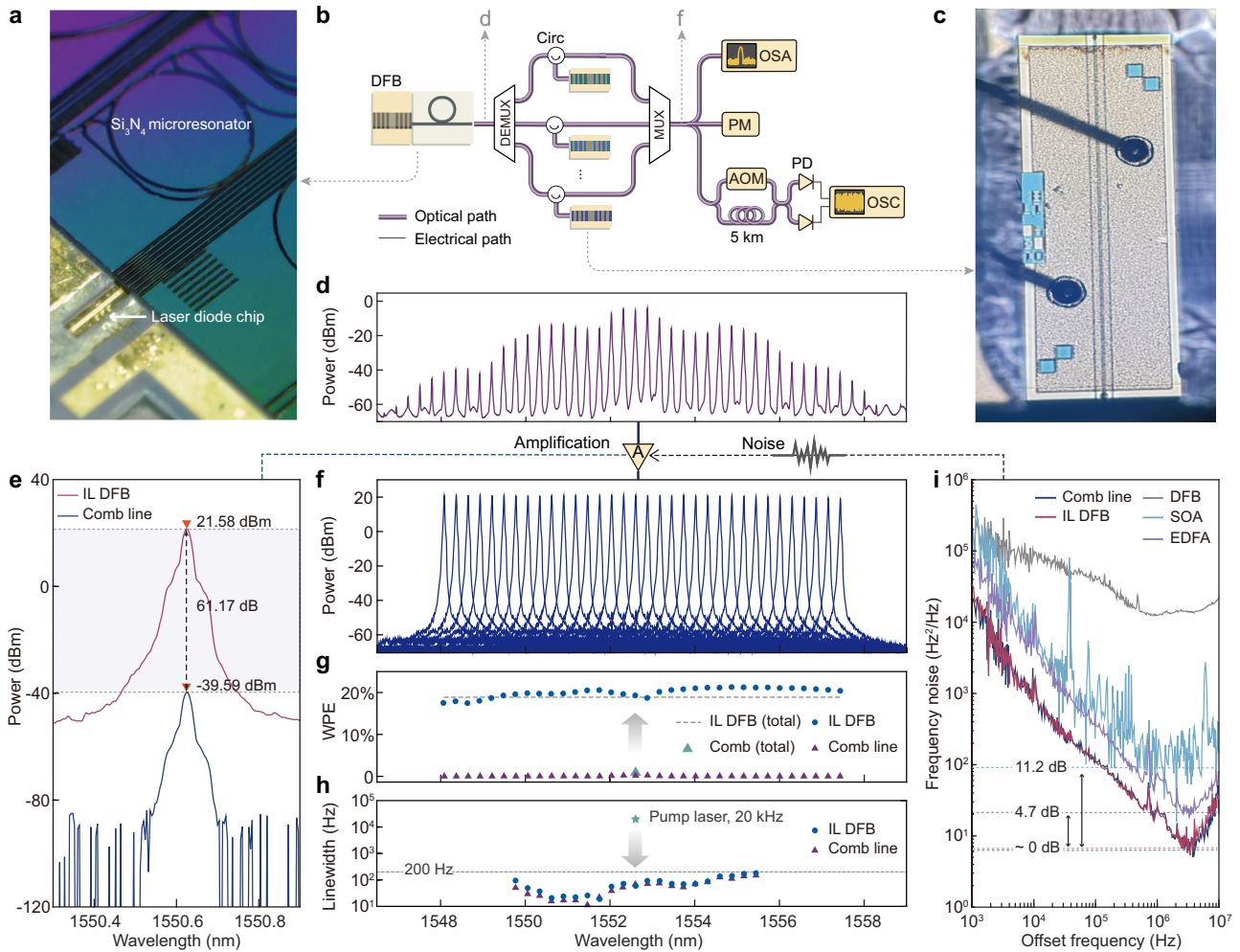


Fig. 2 | Fundamental characteristics of the self-injection locked microcomb and injection locking amplification. **a** Photograph of the integrated DFB laser and a Si₃N₄ microresonator. **b** The link used for fundamental characteristics measurement. DFB distributed feedback laser, DEMUX demultiplexer, Circ circulator, MUX multiplexer, OSA optical spectrum analyzer, PM power meter, AOM acousto-optic modulator, PD photodetector, OSC oscilloscope. **c** Photograph of the slave DFB laser. **d** Spectrum of the microcomb pumped by the self-injection locked DFB laser. **e** Spectra of the comb line at 1550.62 nm before and after injection locking amplification, show that a gain of more than 60 dB can be achieved. **f** Combined spectra of each comb line after being filtered and injection locking amplified. **g** WPE

of different cases. The purple triangles and blue circles represent the WPE of each comb line before and after injection locking amplification. The green triangle represents the overall WPE of the original microcomb. The dashed line represents the overall WPE of all comb lines after amplification including the power supplied to the source DFB laser. **h** Linewidths of different cases. The purple triangles and blue circles represent the intrinsic linewidths of the comb lines before and after injection locking amplification, respectively. Both of them have linewidths below 200 Hz, while the pump DFB laser has a linewidth over 20 kHz. **i** Single-sideband frequency noise of different amplification methods. Injection locking amplification has no significant noise-floor increment.

strong frequency noise reduction of the laser diode^{25,43}. In this work, the microresonator exhibits a high intrinsic Q factor around 4.3×10^7 , which reduces the original 20 kHz intrinsic linewidth of the pump DFB laser to a linewidth down to the 10 Hz level^{44,45}.

The self-injection locking scheme also enables optical frequency comb generation⁴⁶. Since the microresonator is designed for normal dispersion, the microcomb operates in the dark pulse regime^{4,47}, ensuring good coherence over comb lines and distributing narrow-linewidth characteristics among all wavelengths. Our microcomb is pumped by a DFB laser with a power of 19 dBm, and the spectrum of the microcomb is depicted in Fig. 2d. The comb lines exhibit an intrinsic linewidth as low as 11 Hz (Fig. 2h). Our microcomb is among the state-of-the-art integrated optical frequency combs regarding coherency. The microcomb generation is turnkey²⁵ without any auxiliary electronics control, and the comb state can stably last for several hours (Supplementary Note 4).

Secondly, the microcomb serves as a coherence seed to IL DFB lasers (Fig. 2c). We sequentially filter each comb line (master) and

inject it into the free-running DFB laser (slave), thereby locking the frequency of the slave laser (Fig. 2b and Methods). One advantage of this injection locking amplification is its strong power gain and uniform output power. The amplification process is described by the following equation^{48–50} (Supplementary Note 1):

$$S = \frac{S_{fr} - \frac{\gamma_N}{\gamma_p} \Delta N}{1 + \frac{g}{\gamma_p} \Delta N} \quad (1)$$

where γ_N , γ_p , g refer to the carrier recombination rate of the slave laser, photon decay rate, and linear gain coefficient, respectively. ΔN denotes the carrier number difference between the injection locked case and the free-running case. S denotes the intracavity photon number, which is proportional to the output power P . The equation above describes the relationship between injection locked and free-running intracavity photon numbers (S and S_{fr}).

Given the amplification circumstances where $\Delta N \ll 1$, the intra-cavity photon number closely approximates the free-running case, $S \approx S_{fr}$. This indicates that the output power of the slave laser P is nearly the same as its free-running power P_{fr} regardless of the original master light power. This significant amplification effect comes from the cavity enhancement of the slave laser. Injection locking based amplification harnesses the media gain more effectively and thus leads to higher WPE compared with single-pass amplifiers such as the EDFA and the SOA.

To verify this, we attenuate the power of a comb line to a significantly low level before injecting it into a DFB laser, whose free-running power can reach around 21 dBm. The experimental results show that even under the injection power of -39.6 dBm, the slave DFB laser can still be effectively locked and emits a power of 21.6 dBm, indicating an exceptional gain exceeding 61 dB (Fig. 2e). According to our knowledge, such gain value is 30 dB higher than those of other integrated amplifiers^{51,52}. By applying this strategy to each channel of the self-injection locked microcomb and combining them, we obtain a flat spectrum profile (Fig. 2f), with all 34 channels exhibiting a power exceeding 20 dBm. The WPE of each comb line after amplification is nearly the same as the free-running DFB laser, which is significantly higher than the original WPE of each comb line (Fig. 2g and Supplementary Note 6). The overall WPE, which includes the power supplied to the source DFB laser for microcomb generation, is beyond 18.8%. This WPE is almost independent of the original microcomb WPE (1%), since the number of parallel channels is relatively large.

Another appealing property of the injection locking process is the maintenance of high coherence from the seed light. The phase noise after injection locking is described by the following equation⁴⁹(Supplementary Note 1):

$$\begin{aligned} \langle \delta\phi\delta\phi \rangle_{\omega} = & |H_{\phi,\phi_{inj}}(\omega)|^2 \langle \delta\phi_{inj}\delta\phi_{inj} \rangle_{\omega} \\ & + |H_{\phi,\phi}(\omega)|^2 \langle F_{\phi}F_{\phi} \rangle_{\omega} + \Delta \end{aligned} \quad (2)$$

where $\langle \delta\phi_{inj}\delta\phi_{inj} \rangle_{\omega}$ and $\langle F_{\phi}F_{\phi} \rangle_{\omega}$ represent the master light phase fluctuation power spectrum density (PSD) and the slave laser cavity Langevin noise in phase, while Δ represents the phase and photon/carrier number coupling terms that are relatively insignificant in the injection locking process. Specifically, the frequency response of laser cavity Langevin noise $|H_{\phi,\phi}(\omega)|^2$ can be suppressed by more than 40 dB compared with the free-running case, while that of the master light $|H_{\phi,\phi_{inj}}|^2$ remains near 1 in the frequency range of our interest. In other words, the noise factor of the injection locking process is -0 dB.

Here we compare the deterioration of noise under various amplification strategies. We use a comb line with a power of -15.4 dBm and amplify it by 20 dB gain through an EDFA, an SOA and an injection locked DFB laser respectively. Figure 2i displays the single-sideband (SSB) frequency noise spectra of the input and amplified lights. It is observed that the EDFA and the SOA have noise-floor increments of 4.7 dB and 11.2 dB, respectively, whereas the injection locking amplification shows no appreciable increase in the noise-floor. Compared with the EDFA and the SOA case in which the amplification effect accumulates along propagation, the light field circulates and gets enhanced in the slave laser cavity. Consequently, more carriers are involved in stimulated emission rather than spontaneous emission, resulting in reduced additional amplified spontaneous emission noise and better phase noise performance. We further measure the intrinsic linewidths of the injection locking amplified comb lines, each at an output power of about 20 dBm. It is shown that the coherence of the original microcomb is preserved over the spectrum (Fig. 2h and methods).

High-capacity parallel communications with silicon photonic transceivers

This power-efficient, high-coherence parallel source can significantly enhance the performance of coherent systems on PICs and enable

complex system functionality. Here, we use it to drive SiPh transceivers in a high-speed coherent optical communication system. Figure 3a illustrates the system architecture. The transmitter necessitates an optical power of more than 15 dBm to accommodate advanced modulation formats. To meet this requirement, each comb line is separated into different channels by a fiber Bragg grating filter (FBG) and amplified to a uniform power of about 20 dBm by injection locking DFB lasers, with an optical signal to noise ratio exceeding 70 dB. Within each channel, the amplified light is divided into two parts. One, serving as a data carrier, holds 99% of the power and undergoes modulation by a SiPh transmitter, while the other remains unmodulated, retaining only 1% of the power, and functions as the local oscillator (LO). The modulated data channels are combined by a multiplexer, and so are the LOs. To ensure high coherence for homodyne detection, the signals and the LOs are transmitted concurrently^{42,53}. At the receiver side, the combined signal lights and LOs are separated into different wavelength channels and detected separately. To satisfy the power requirements of the receiver and further enhance detection accuracy, the LOs are boosted to -20 dBm by injection locking other DFB lasers. Thanks to the ample power and excellent coherence, our approach can effectively facilitate wavelength division multiplexing (WDM) coherent transmission of high capacity and advanced modulation formats.

It is noteworthy that both the transmitter and the receiver utilized in our experimental setup are silicon-on-insulator (SOI) based and manufactured by a commercial CMOS foundry, as depicted in Fig. 3a. The transmitter comprises two IQ modulators, one polarization rotator and beam combiner (PRBC), two monitor photodetectors (MPD) and associated drivers. The receiver includes dual 90° optical hybrids, one polarization rotator and beam splitter (PRBS), two MPDs, variable optical attenuators (VOA), four high-speed balanced-photodiodes (BPD), and trans-impedance amplifiers (TIA). Among them, the PRBS and the PRBC are used to implement on-chip polarization multiplexing. We have optically and electrically packaged the SiPh transmitter and receiver, which possess electro-optic bandwidth and optoelectrical bandwidth of around 50 GHz, respectively. Our transmitter and receiver are capable of covering the entire wavelength span of the microcomb, enabling the demonstration of all channels with the same equipment.

We employ dual-polarization 32-state quadrature amplitude modulation (DP-32-QAM) at a symbol rate of 30 Gbaud to encode data on each of the 34 amplified comb lines. Consequently, each modulated channel achieves a data rate of 300 Gbit/s ($30 \text{ Gbaud} \times 5 \text{ bits} \times 2 \text{ polarizations}$), resulting in an overall data rate of 10.2 Tbit/s across the 34 channels. Moreover, we utilize a 1-km-long 7-core fiber, with 6 cores allocated for transmitting the modulated lights and 1 core dedicated to transmitting the LOs at minimal power levels. After signal recovery at the receiver side, the calculated bit error ratios (BER) of all channels remain below 5.6×10^{-4} (Fig. 3c), much lower than the 7% hard-decision forward error correction threshold of 3.8×10^{-3} . Figure 3d displays the constellation diagrams of recovered dual-polarization data for all channels in cores 1–6 after transmission (Supplementary Note 9). The clear constellation diagrams of all channels demonstrate the excellent behavior of our approach in advanced coherent modulated formats. Finally, we validate a silicon-based coherent WDM transmission experiment with an aggregate gross line rate of 61.2 Tbit/s and a net spectral efficiency of 8.01 bit/s/Hz (Fig. 3b). According to our knowledge, this is the record number for a coherent link based on integrated sources and SiPh transceivers, marking a rate 30 times higher than that of the existing SiPh links⁴.

DSP reduction in integrated high-coherence parallel system

Besides the hardware breakthrough, this parallel approach can also bring significant DSP reduction in coherent systems. Conventional coherent communication systems usually use DFB lasers to generate optical carriers and LOs, whose frequencies and phases vary rapidly

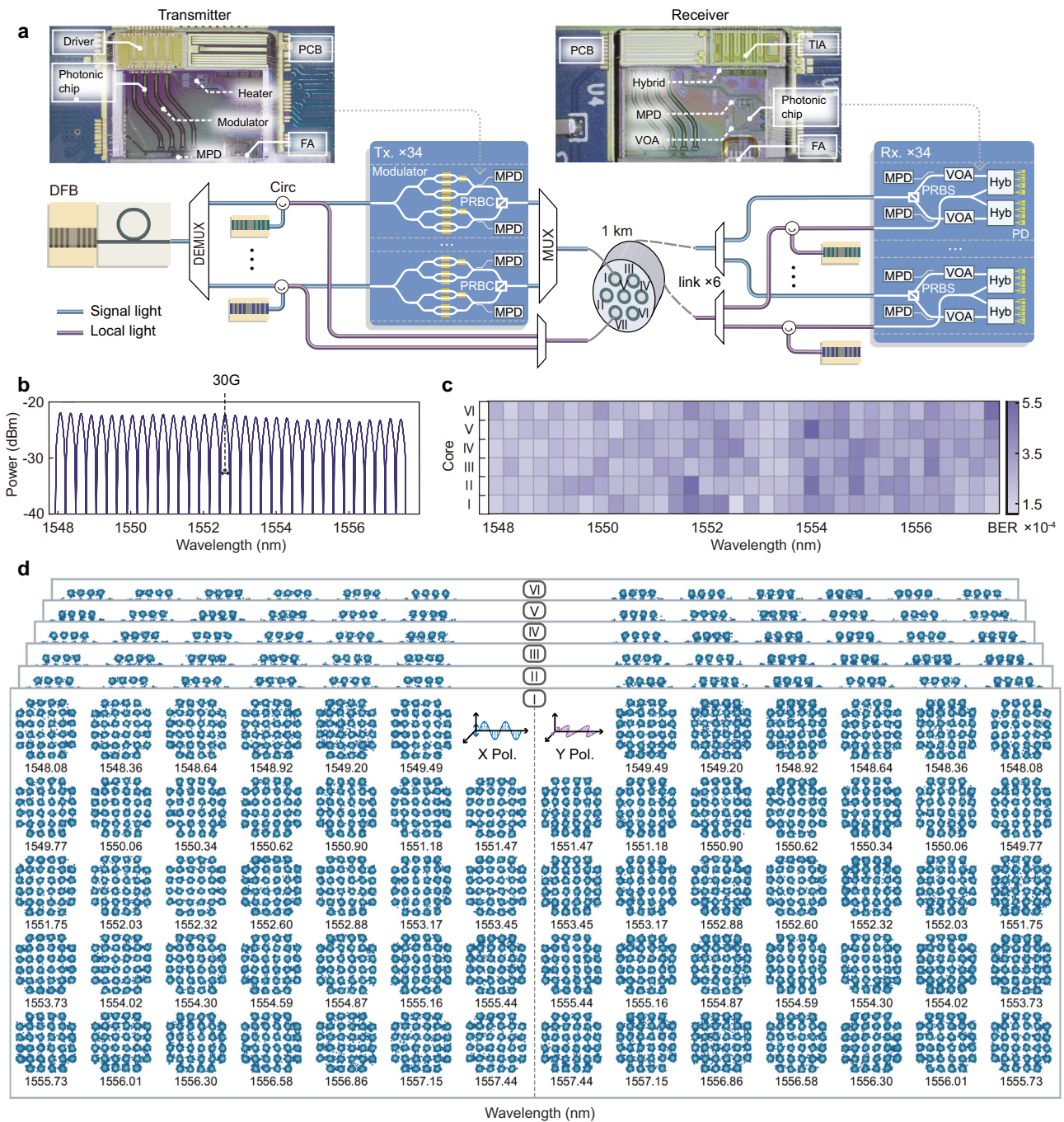


Fig. 3 | Parallel coherent silicon photonic communications. **a** Architecture of the coherent communication system utilizing our power-efficient, high-coherence parallel source. Photographs of the transmitter and receiver chips are shown at the top. Tx transmitter, Rx receiver, PRBC polarization rotator and beam combiner, PRBS polarization rotator and beam splitter, MPD monitor

photodetector, VOA variable optical attenuator, Hyb 90° hybrid, FA fiber array, TIA trans-impedance amplifier. **b** Combined spectra of modulated carriers for all 34 channels. **c** BERs across 34 wavelengths and 6 cores. **d** Recovered constellation diagrams across 34 channels and 6 cores. X Pol X polarization, Y Pol Y polarization.

and randomly. Consequently, unpredictable frequency offsets and phase fluctuations arise between carriers and LOs, as depicted in Fig. 4b(i). To accurately recover the signal, frequency offset estimation (FOE) and carrier phase estimation (CPE) become necessary. This brings additional DSP requirements for coherent communications compared to intensity modulation direct detection systems, consequently leading to higher power consumption.

There are two key advantages of our strategy for saving the DSP. Firstly, the source itself exhibits a narrow linewidth.

Secondly, our strategy preserves coherence during amplification, allowing for the transmission of low-power carriers. The coherent communication link and DSP modules we use are illustrated in Fig. 4a. In our strategy, there is no frequency offset, and the phase fluctuations between the signal carrier and the LO are significantly mitigated, as illustrated in Fig. 4c (i). Consequently, FOE can be entirely omitted. Moreover, by simply estimating the initial phase and applying it to subsequent data, we can still maintain relatively high performance.

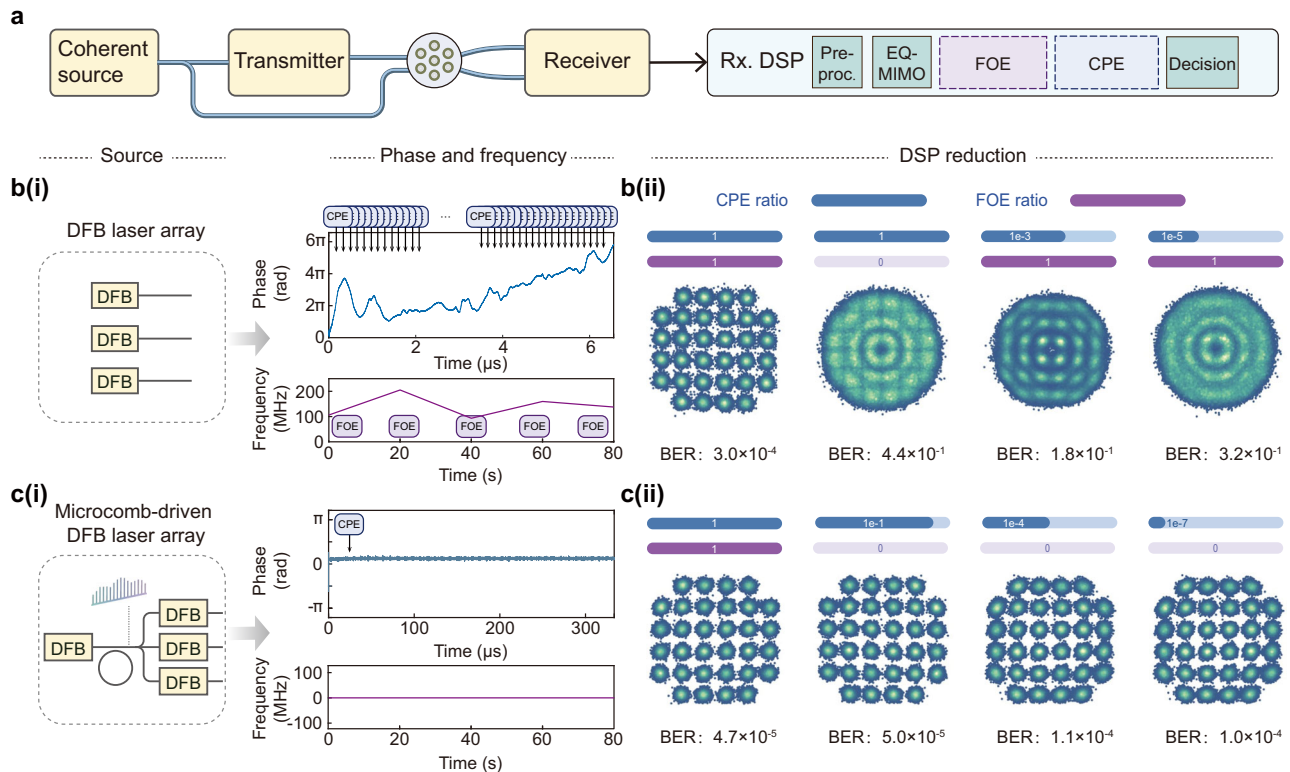


Fig. 4 | DSP reduction induced by high-coherence parallelization. a Brief architecture and DSP modules in our strategy. Pre-proc pre-processing, EQ-MIMO equalization multiple-input-multiple-output, FOE frequency offset estimation, CPE carrier phase estimation. **b (i)** Using standalone DFB lasers as the carrier and the LO, both the frequency offset and the phase difference change rapidly, requiring frequent CPE and FOE in DSP. **b (ii)** DSP reduction results in the degradation of

constellation diagrams when using standalone DFB lasers. **c (i)** In our scheme, the frequency offset is 0, and the phase difference is stable. Therefore, we can significantly reduce the CPE ratio and omit FOE. **c (ii)** Recovered constellation diagrams are well maintained with different ratios of CPE and FOE when using our strategy.

To demonstrate the impact of reducing the usage of coherent DSP, we apply different ratios of FOE and CPE to a 30 GBaud 32-QAM coherent transmission link (Methods). The CPE ratio represents the number of CPE operations we perform compared to the traditional algorithm, which executes a CPE operation on every symbol. We also compare the BERs of our strategy with the scheme using two standalone DFB lasers as the carrier and the LO. Both schemes recover the signal successfully when employing full coherent-related DSP which incorporates FOE once and CPE for every symbol. Utilizing two standalone DFB lasers results in a BER of 3.0×10^{-4} , whereas our strategy achieves a significantly lower BER of 4.7×10^{-5} . Furthermore, in the case of using standalone DFB lasers without FOE, it is hard to recover data due to the presence of intolerable frequency deviations. When we decrease the normalized ratio of CPE while retaining FOE, a CPE ratio of 1×10^{-3} results in a BER of 1.8×10^{-1} . As the CPE ratio continues to decrease to 1×10^{-5} , data recovery becomes nearly impossible (Fig. 4b(ii)). In our scheme, we can remove the FOE and substantially reduce the CPE ratio. We gradually reduce the CPE ratio to 1×10^{-7} , meaning we run CPE once every other 1×10^7 data blocks. Despite this reduction, we still achieve successful data recovery, demonstrating a BER performance of 1.0×10^{-4} , which is comparable to that of a full DSP (Fig. 4c(ii)). Notably, the minimum required CPE ratio is currently only limited by the length of our data within a time window. The comparison between the two schemes highlights the strong performance of our strategy, capable of reducing full FOE and 99.99999% of the CPE. We also conduct transmission experiments using a 12-km-long fiber. Our architecture still achieves the same level of DSP reduction (Supplementary Note 11), showing that it can be used in inter-datacenter optical interconnects.

Discussion

By utilizing microcombs with many more channels and broader spans as we demonstrated before⁵⁴, the level of parallelization can be significantly improved. In our experiment, we employ a filter to select each comb line for the WDM purpose, which can later be substituted by other integrated components, such as arrayed waveguide gratings. It is noteworthy that the circulator in our scheme currently prevents us from integrating the microcomb with the DFB laser array. However, for injection locking, circulators or isolators might not be necessary, as we have demonstrated that the microresonator can simultaneously achieve isolation^{55,56} and mitigate the impact of reflected light. We envisage that despite potential challenges such as the effects of reflected light, employing a power splitter^{57,58} or injecting light through the rear facet of the laser⁵⁹ may serve a similar function and is more integration-friendly.

Beyond delivering exceptional performance, our strategy offers compatibility with the existing photonic ecosystem. The III-V laser array has been extensively used in photonic transceivers⁶⁰, LiDAR⁶¹ and computation units⁶², and the transition to our highly-coherent source only takes one chip-based comb generator. Importantly, all the key components in our systems are chip-based and manufactured from photonic foundries. Our recent advancements in heterogeneous fabrication technology enable the integration of all these components on the same substrate, supporting mass production^{26,63,64}. The simplification of the coherent DSP, together with the emergence of the linear-drive pluggable optics technologies, paves the way for a DSP-light coherent system with great energy efficiency.

Our method can be extended to diverse applications beyond communications. For FMCW LiDAR, achieving more than 20-dBm power at multiple channels with high coherence is critical for long-

distance ranging in automobiles with a fast scan rate⁶⁵. The high-power, high-coherence parallelization can also improve the signal-to-noise ratio in computation PICs, particularly when thousands of cascaded Mach-Zehnder interferometers introduce large losses⁶. We also expect this strategy to facilitate the $f-2f$ self-reference process^{54,66,67} by boosting the power for nonlinear frequency conversions, which will benefit optical synthesizers²² and optical clocks⁶⁸ on chip.

Methods

Fabrication of Si₃N₄ microresonator

The Si₃N₄ microresonator is fabricated in a commercial CMOS foundry. The starting material consists of a 200 mm diameter silicon wafer featuring 14.5 μm of thermally-oxidized SiO₂ on its surface. The waveguide is formed by low-pressure chemical vapor deposition (LPCVD) of Si₃N₄, followed by deep-UV lithography and plasma etching for pattern transfer. The resultant Si₃N₄ core is then capped by 4 μm of SiO₂, formed using LPCVD with a tetraethyl orthosilicate precursor and annealing at 1150 °C. The resultant wafer is singulated into chips using a blade dicing saw.

Generation of the self-injection locked microcomb

We mount a DFB laser chip with an output power of 19 dBm in a butterfly package on a 6-axis stage (Thorlabs MAX602D/M). The Si₃N₄ chip is placed on a thermoelectric cooler holder, whose temperature is controlled by a temperature controller (Vescent SLICE-QTC) to keep the Si₃N₄ chip in a stable state. We use a laser diode controller (Thorlabs ITC4001) to adjust the temperature of the DFB laser diode (LD) and provide the drive current. By using a piezo controller (Thorlabs MDT693B) to control the 6-axis stage, the relative position between the DFB laser and the Si₃N₄ chip can be accurately controlled so that the two chips can be closely butt-coupled. By setting the temperature and current of the DFB laser to the appropriate values, the DFB laser can be self-injection locked, leading to the generation of a microcomb at the through port of the microresonator²⁵. The generation of the microcomb can be realized by simply turning on the drive current of the DFB laser, which is known as the turnkey operation. A lensed fiber fixed on a 3-axis stage (Thorlabs MAX312D/M) is used to collect the output light from the Si₃N₄ chip. We record the generated microcomb with an optical spectrum analyzer (Yokogawa AQ6370D). By controlling the OSA to periodically store the spectra at 20-s intervals, we characterize the long-term stability of the microcomb over 2 h.

Characterization of the microcomb before and after amplification

We use a tunable fiber Bragg grating filter (AOS Tunable FBG) to filter one of the comb lines. A total of six DFB lasers are used to amplify comb lines of different wavelengths and these DFB lasers are all free-running without any active stabilization. After adjusting the polarization of the light through a PC (Thorlabs FPC560), we inject it into a DFB laser through a polarization maintaining circulator (PMC) to achieve injection locking amplification. Given the limited number of DFB laser chips, we adjust the temperature of each DFB laser to modify the output wavelength, enabling the system to achieve amplification of each comb line. The PM (Thorlabs PM100D) and the OSA are employed to acquire the power and spectral variations before and after injection locking, respectively. By observing the change in the output frequency from the OSA while adjusting the temperature of the DFB laser chip, we can ascertain whether the DFB laser is injection locked. To measure the frequency noise before and after injection locking, the correlated self-heterodyne method is adopted⁴⁵. We firstly split the light into two paths: one path passes through an acousto-optic modulator (AOM, Gooch&Housego T-M080-0.4C2J-3-F2P) with a frequency shift of 80 MHz, while the other is delayed by a 5-km-long fiber with a polarization controller. The light is then recombined and split into two beams of equal power received by two identical PDs (Newport 1811-

FC). The outputs of PDs are recorded using a high-speed oscilloscope (Keysight MXR404A) with a sampling rate of 500 MSa/s. A waveform of 0.2 s is collected and analyzed by a computer. We compare and plot the frequency noise generated using different amplification methods: an EDFA (Amonics AEDFA-C-DWDM), an SOA (Thorlabs SOA1117S) and an injection locked DFB laser. Considering that sufficient optical power is needed to make the PD respond efficiently, we measure the linewidth of 21 comb lines of the microcomb. By comparing the linewidth before and after injection locking amplification, we observe that minimal noise is introduced.

Coherent communication details

After being filtered in turn, each comb line passes through a PC and is split into two paths using a polarization maintaining power splitter. One path, with 1% of the power, connects to a PM for monitoring the polarization of light to ensure effective injection locking. Another path, carrying 99% of the power passes through a PMC to IL the DFB laser. A very small fraction of the output light from the injection locked laser is split off and monitored by the OSA. The remaining light is modulated with the data generated by an arbitrary waveform generator (Keysight M8194A). The power of the input carrier is 17 dBm, while the power of the output signal light is -13.4 dBm. The modulated signal light and the unmodulated LO are transmitted concurrently through two distinct cores of the 7-core fiber. The fiber exhibits an attenuation loss of 0.25 dB/km, an inter-core crosstalk of less than -60 dB, and a dispersion of about 17.1 ps/(nm km). The LO power at the receiver side is -9.8 dBm, which is then amplified to 20 dBm by injection locking another DFB laser with a similar structure. The signal light, with a power of -15.1 dBm, is sent to the coherent receiver together with the LO light. The receiver is powered by a DC power supply (Keysight E36312A). The electrical signals generated by the receiver through the beating of the signal light with the LO are captured by a high-performance real-time oscilloscope after passing through DC blocks (Gwave GDCB-67G-185) and baluns (HYPERLABS HL9407), respectively. The OSC can provide a conversion rate of 80 GSa/s and a bandwidth of 33 GHz on four simultaneous channels. The data samples we collect at a time last for up to 334 μs, as determined by the maximum memory depth of the OSC we use, and are subsequently processed by a computer for DSP.

Digital signal processing

In the DSP at the receiver side, the sampled signal is first orthogonally normalized using the Gram-Schmidt algorithm to compensate for the effects of non-ideal factors in the link³⁶. Continuing with the process, we apply matched filter to the signal using a root-raised cosine filter with a roll-off coefficient of 0.05, followed by downsampling the signal from 80 GSa/s to 30 GSa/s. Subsequently, adaptive equalization and carrier recovery are performed. The equalizer adopts a 4 × 2 multiple-input multiple-output structure. We employ the constant modulus algorithm (CMA) to achieve pre-convergence of the taps in the equalizer. The output signal from CMA is then utilized for FOE. FOE is accomplished by taking the signal to the fourth power and identifying the highest spectral peak. After this, a decision-directed approach is employed for equalization. In equalization, CPE is executed using the blind phase search algorithm with 16 test angles. After equalization and carrier recovery, orthogonalization is employed to address both hybrid imperfections and modulator bias issues. Finally, symbol decisions are made and BERs are calculated to assess the system performance.

Design and fabrication of the transceiver

The transmitter and receiver are both SOI-based SiPh integrated chips. At the transmitter side, the optical carrier is split on chip into two paths that pass through two IQ modulators. To maintain the correct operating state, the modulators are monitored by MPDs and adjusted by

heaters. The drivers are used to drive the modulators to load electrical signals onto the optical carriers. Two paths of modulated lights go into the PRBC to generate a dual-polarized IQ-modulated signal, which is then coupled into the optical fiber through an FA for transmission. At the receiver side, the signal light and the LO are coupled to the receiver chip via an FA. The PRBS splits the signal light into two polarization-orthogonal paths. The power of each path is monitored by MPDs and adjusted by VOAs. The signal lights and LOs are mixed in 90° optical hybrids and converted to photocurrent by BPDs. The current is amplified and converted to voltage output by TIAs.

Data availability

The data that supports the plots within this paper and other findings of this study are available on Zenodo (<https://doi.org/10.5281/zenodo.13162905>). All other data used in this study are available from the corresponding authors upon request.

Code availability

The codes that support the findings of this study are available from the corresponding authors upon request.

References

- Pfeifle, J. et al. Coherent terabit communications with micro-resonator Kerr frequency combs. *Nat. Photonics* **8**, 375–380 (2014).
- Marin-Palomo, P. et al. Microresonator-based solitons for massively parallel coherent optical communications. *Nature* **546**, 274–279 (2017).
- Yang, K. Y. et al. Multi-dimensional data transmission using inverse-designed silicon photonics and microcombs. *Nat. Commun.* **13**, 7862 (2022).
- Shu, H. et al. Microcomb-driven silicon photonic systems. *Nature* **605**, 457–463 (2022).
- Rizzo, A. et al. Massively scalable Kerr comb-driven silicon photonic link. *Nat. Photonics* **17**, 781–790 (2023).
- Shen, Y. et al. Deep learning with coherent nanophotonic circuits. *Nat. Photonics* **11**, 441–446 (2017).
- Feldmann, J. et al. Parallel convolutional processing using an integrated photonic tensor core. *Nature* **589**, 52–58 (2021).
- Xu, X. et al. 11 TOPS photonic convolutional accelerator for optical neural networks. *Nature* **589**, 44–51 (2021).
- Ashtiani, F., Geers, A. J. & Aflatouni, F. An on-chip photonic deep neural network for image classification. *Nature* **606**, 501–506 (2022).
- Wang, J., Sciarrino, F., Laing, A. & Thompson, M. G. Integrated photonic quantum technologies. *Nat. Photonics* **14**, 273–284 (2020).
- Pelucchi, E. et al. The potential and global outlook of integrated photonics for quantum technologies. *Nat. Rev. Phys.* **4**, 194–208 (2022).
- Riemensberger, J. et al. Massively parallel coherent laser ranging using a soliton microcomb. *Nature* **581**, 164–170 (2020).
- Chen, R. et al. Breaking the temporal and frequency congestion of LiDAR by parallel chaos. *Nat. Photonics* **17**, 306–314 (2023).
- Li, B., Lin, Q. & Li, M. Frequency-angular resolving LiDAR using chip-scale acousto-optic beam steering. *Nature* **620**, 316–322 (2023).
- Dong, P. et al. Monolithic silicon photonic integrated circuits for compact 100+ Gb/s coherent optical receivers and transmitters. *IEEE J. Sel. Top. Quantum Electron.* **20**, 150–157 (2014).
- Martin, A. et al. Photonic integrated circuit-based FMCW coherent LiDAR. *J. Lightwave Technol.* **36**, 4640–4645 (2018).
- Fülöp, A. et al. High-order coherent communications using mode-locked dark-pulse Kerr combs from microresonators. *Nat. Commun.* **9**, 1598 (2018).
- Corcoran, B. et al. Ultra-dense optical data transmission over standard fibre with a single chip source. *Nat. Commun.* **11**, 2568 (2020).
- Lundberg, L. et al. Phase-coherent lightwave communications with frequency combs. *Nat. Commun.* **11**, 201 (2020).
- Xu, M. et al. Dual-polarization thin-film lithium niobate in-phase quadrature modulators for terabit-per-second transmission. *Optica* **9**, 61–62 (2022).
- Jørgensen, A. et al. Petabit-per-second data transmission using a chip-scale microcomb ring resonator source. *Nat. Photonics* **16**, 798–802 (2022).
- Spencer, D. T. et al. An optical-frequency synthesizer using integrated photonics. *Nature* **557**, 81–85 (2018).
- Liu, S. et al. High-power single-longitudinal-mode DFB semiconductor laser based on sampled Moiré grating. *IEEE Photonics Technol. Lett.* **31**, 751–754 (2019).
- Vaskasi, J. R. et al. High wall-plug efficiency and narrow linewidth III-V-on-silicon C-band DFB laser diodes. *Opt. Express* **30**, 27983–27992 (2022).
- Shen, B. et al. Integrated turnkey soliton microcombs. *Nature* **582**, 365–369 (2020).
- Xiang, C. et al. Laser soliton microcombs heterogeneously integrated on silicon. *Science* **373**, 99–103 (2021).
- Stern, B., Ji, X., Okawachi, Y., Gaeta, A. L. & Lipson, M. Battery-operated integrated frequency comb generator. *Nature* **562**, 401–405 (2018).
- Xue, X., Wang, P.-H., Xuan, Y., Qi, M. & Weiner, A. M. Microresonator Kerr frequency combs with high conversion efficiency. *Laser Photonics Rev.* **11**, 1600276 (2017).
- Li, J. et al. Efficiency of pulse pumped soliton microcombs. *Optica* **9**, 231–239 (2022).
- Helgason, Ó. B. et al. Surpassing the nonlinear conversion efficiency of soliton microcombs. *Nat. Photonics* **17**, 992–999 (2023).
- Raja, A. S. et al. Ultrafast optical circuit switching for data centers using integrated soliton microcombs. *Nat. Commun.* **12**, 5867 (2021).
- Wu, D. S., Slavik, R., Marra, G. & Richardson, D. J. Direct selection and amplification of individual narrowly spaced optical comb modes via injection locking: design and characterization. *J. Lightwave Technol.* **31**, 2287–2295 (2013).
- Zhang, Q. et al. Low-noise amplification of dissipative Kerr soliton microcomb lines via optical injection locking lasers. *Chin. Opt. Lett.* **19**, 121401 (2021).
- Heffernan, B. M. et al. 60 Gbps real-time wireless communications at 300 GHz carrier using a Kerr microcomb-based source. *APL Photonics* **8**, 066106(2023).
- Pillai, B. S. G. et al. End-to-end energy modeling and analysis of long-haul coherent transmission systems. *J. Lightwave Technol.* **32**, 3093–3111 (2014).
- Faruk, M. S. & Savory, S. J. Digital signal processing for coherent transceivers employing multilevel formats. *J. Lightwave Technol.* **35**, 1125–1141 (2017).
- Crivelli, D. E. et al. Architecture of a single-chip 50 Gb/s DP-QPSK/BPSK transceiver with electronic dispersion compensation for coherent optical channels. *IEEE Trans. Circuits Syst. I: Regul. Pap.* **61**, 1012–1025 (2013).
- Tauber, D. et al. Role of coherent systems in the next DCI generation. *J. Lightwave Technol.* **41**, 1139–1151 (2023).
- Brodnik, G. M. et al. Optically synchronized fibre links using spectrally pure chip-scale lasers. *Nat. Photonics* **15**, 588–593 (2021).
- Geng, Y. et al. Coherent optical communications using coherence-cloned Kerr soliton microcombs. *Nat. Commun.* **13**, 1070 (2022).
- Zhang, C. et al. Clone-comb-enabled high-capacity digital-analogue fronthaul with high-order modulation formats. *Nat. Photonics* **17**, 1000–1008 (2023).
- Puttnam, B. et al. C+ L-band seeded comb regeneration for MCF networks. In *Proc. 49th European Conference on Optical Communications (ECOC 2023)*, vol. 2023, 393–396 (IET, 2023).

43. Jin, W. et al. Hertz-linewidth semiconductor lasers using CMOS-ready ultra-high-Q microresonators. *Nat. Photonics* **15**, 346–353 (2021).
44. Camatel, S. & Ferrero, V. Narrow linewidth CW laser phase noise characterization methods for coherent transmission system applications. *J. Lightwave Technol.* **26**, 3048–3055 (2008).
45. Yuan, Z. et al. Correlated self-heterodyne method for ultra-low-noise laser linewidth measurements. *Opt. Express* **30**, 25147–25161 (2022).
46. Chang, L., Liu, S. & Bowers, J. E. Integrated optical frequency comb technologies. *Nat. Photonics* **16**, 95–108 (2022).
47. Xue, X. et al. Mode-locked dark pulse Kerr combs in normal-dispersion microresonators. *Nat. Photonics* **9**, 594–600 (2015).
48. Lang, R. Injection locking properties of a semiconductor laser. *IEEE J. Quantum Electron.* **18**, 976–983 (1982).
49. Lau, E. K., Wong, L. J. & Wu, M. C. Enhanced modulation characteristics of optical injection-locked lasers: a tutorial. *IEEE J. Sel. Top. Quantum Electron.* **15**, 618–633 (2009).
50. Liu, Z. & Slavik, R. Optical injection locking: from principle to applications. *J. Lightwave Technol.* **38**, 43–59 (2020).
51. Sobhanan, A. et al. Semiconductor optical amplifiers: recent advances and applications. *Adv. Opt. Photonics* **14**, 571–651 (2022).
52. Liu, Y. et al. A photonic integrated circuit-based erbium-doped amplifier. *Science* **376**, 1309–1313 (2022).
53. Puttnam, B. J., Luis, R. S., Awaji, Y. & Wada, N. Self-homodyne and phase measurements for MCF transmission with wideband comb transmitter. In *Proc. IEEE Photonics Conference (IPC)*, 299–300 (IEEE, 2016).
54. Briles, T. C. et al. Hybrid InP and SiN integration of an octave-spanning frequency comb. *APL Photonics* **6**, 026102 (2021).
55. White, A. D. et al. Integrated passive nonlinear optical isolators. *Nat. Photonics* **17**, 143–149 (2023).
56. White, A. D. et al. Unified laser stabilization and isolation on a silicon chip. *arXiv preprint arXiv:2404.03093* (2024).
57. Zhou, R., Shao, T., Pascual, M. D. G., Smyth, F. & Barry, L. P. Injection locked wavelength de-multiplexer for optical comb-based Nyquist WDM system. *IEEE Photonics Technol. Lett.* **27**, 2595–2598 (2015).
58. Liu, Z., Farwell, S., Wale, M., Richardson, D. J. & Slavik, R. InP-based optical comb-locked tunable transmitter. In *Proc. Optical Fiber Communication Conference*, Tu2K-2 (Optica Publishing Group, 2016).
59. Albores-Mejia, A. et al. Optical-comb-line selection from a low-power/low-OSNR comb using a low-coherence semiconductor laser for flexible ultra-dense short range transceivers. In *Proc. Optical Fiber Communications Conference and Exhibition (OFC)*, 1–3 (IEEE, 2015).
60. Yang, M. et al. Single-carrier 800-Gb/s self-homodyne coherent transmission of DP-16QAM, DP-32QAM, and DP-64QAM with uncooled DFB laser. *Opt. Express* **31**, 27553–27565 (2023).
61. DiLazaro, T. & Nehmetallah, G. Multi-terahertz frequency sweeps for high-resolution, frequency-modulated continuous wave radar using a distributed feedback laser array. *Opt. Express* **25**, 2327–2340 (2017).
62. Nahmias, M. A. et al. A TeraMAC neuromorphic photonic processor. In *Proc. IEEE Photonics Conference (IPC)*, 1–2 (IEEE, 2018).
63. Liang, D. et al. An energy-efficient and bandwidth-scalable DWDM heterogeneous silicon photonics integration platform. *IEEE J. Sel. Top. Quantum Electron.* **28**, 1–19 (2022).
64. Tran, M. A. et al. Extending the spectrum of fully integrated photonics to submicrometre wavelengths. *Nature* **610**, 54–60 (2022).
65. Zhang, G. et al. Demonstration of high output power DBR laser integrated with SOA for the FMCW LiDAR system. *Opt. Express* **30**, 2599–2609 (2022).
66. Del’Haye, P. et al. Phase-coherent microwave-to-optical link with a self-referenced microcomb. *Nat. Photonics* **10**, 516–520 (2016).
67. Okawachi, Y. et al. Chip-based self-referencing using integrated lithium niobate waveguides. *Optica* **7**, 702–707 (2020).
68. Newman, Z. L. et al. Architecture for the photonic integration of an optical atomic clock. *Optica* **6**, 680–685 (2019).

Acknowledgements

L.C. acknowledges the National Key Research and Development Program of China (Grant No. 2021YFB2801200), the Beijing Municipal Science & Technology Commission, Administrative Commission of Zhongguancun Science Park (Grant No. Z231100006023007), the Beijing Municipal Natural Science Foundation (Grant No. Z220008), and the National Natural Science Foundation of China (Grant No. 12293052). We thank Chenbo Zhang, Xinyu Chen and Mingqing Zuo for helpful discussions. We thank Weilin Xie, Zhongwei Tan and Yi Dong for their help with the experiments. The experiments are supported by High-performance Computing Platform of Peking University.

Author contributions

The concept of this work was conceived by X.Z., L.C. and X.W. The experiments were performed by X.Z., Z.Z. and Y.G., with the assistance of M.Z., W.J., B.S., H.S., Y.C., J.H., Z.T., M.J., R.C., Z.G., Z.F., N.Z., Y.L., P.C., W.H. and D.P. The results were analyzed by X.Z., Z.Z., Y.G. and M.Z. All authors participated in the writing of the manuscript. The project was under the supervision of L.C., X.W. and J.E.B.

Competing interests

The authors declare no competing interests.

Additional information

Supplementary information The online version contains supplementary material available at <https://doi.org/10.1038/s41467-024-52269-7>.

Correspondence and requests for materials should be addressed to John E. Bowers, Xingjun Wang or Lin Chang.

Peer review information *Nature Communications* thanks the anonymous reviewer(s) for their contribution to the peer review of this work. A peer review file is available.

Reprints and permissions information is available at <http://www.nature.com/reprints>

Publisher’s note Springer Nature remains neutral with regard to jurisdictional claims in published maps and institutional affiliations.

Open Access This article is licensed under a Creative Commons Attribution-NonCommercial-NoDerivatives 4.0 International License, which permits any non-commercial use, sharing, distribution and reproduction in any medium or format, as long as you give appropriate credit to the original author(s) and the source, provide a link to the Creative Commons licence, and indicate if you modified the licensed material. You do not have permission under this licence to share adapted material derived from this article or parts of it. The images or other third party material in this article are included in the article’s Creative Commons licence, unless indicated otherwise in a credit line to the material. If material is not included in the article’s Creative Commons licence and your intended use is not permitted by statutory regulation or exceeds the permitted use, you will need to obtain permission directly from the copyright holder. To view a copy of this licence, visit <http://creativecommons.org/licenses/by-nc-nd/4.0/>.

© The Author(s) 2024